Understanding the fretting corrosion mechanism of zirconium alloy exposed to high temperature high pressure water

Xianglong Guo[a], Ping Lai[a], Zhao Shen[b,c*], Wenhua Zhuang[a], Zhongli Han[a], Lefu Zhang[a*], Sergio Lozano-Perez[c]

[a] School of Nuclear Science and Engineering, Shanghai Jiao Tong University, 800 Dongchuan Road, Shanghai 200240, China
[b] School of Materials Science and Engineering, Shanghai Jiao Tong University, 800 Dongchuan Road, Shanghai 200240, China
[c] Department of Materials, University of Oxford, Parks Road, OX1 3PH Oxford, UK
*Corresponding author: 952911809@qq.com, lfzhang@sjtu.edu.cn

Abstract: The fretting corrosion behaviors of as received and shot peened zirconium alloys in high temperature high pressure water have been studied. The results show that shot peening increases the wear resistance of the materials, changing the wear mode from abrasive wear plus delamination to abrasive wear. The coupling effects of mechanical wear and chemical corrosion on the failure mechanism of the two materials are revealed by advanced characterization and mechanical analysis. It is found that debris buildup and abrasive areas are formed on the fretting surface. The mechanical wear promotes the corrosion of zirconium alloys by forming a thick dual-layer structure oxide scale in the debris buildup area. Next, the oxide scale in the abrasive area is worn, which reduces the protectiveness of the oxide scale. However, the effects of corrosion on the mechanical wear are controversial, and it is dependent on the compactness of the oxide scale formed in the fretting wear process. The cyclic frictional force acting on the surface of the zirconium alloy is too small to initiate cracks in the materials without defects. But the internal stress originating from corrosion results in the formation of cracks in the oxide scale. For the shot peened specimen, the residual stress originating from shot peening accelerates the formation of cracks due to the higher shear stress in the oxide layer. Those cracks propagate under cyclic frictional forces in the fretting wear process and finally result in the delamination of the materials.

Key words: Zirconium alloy, Shot peening, Fretting wear, Corrosion, Cracks

1 Introduction

Among the various energy sources, nuclear energy is the most efficient one to replace fossil fuel and reduce carbon dioxide emission all over the world [1]. Especially in developing countries, the nuclear power accounts for a relatively low portion of the electric power supply, for example, ~4 % in China in the year of 2018 [2]. To promote the development of nuclear energy industry and achieve the role of reducing carbon dioxide emission in the future, keeping the safe operation of nuclear reactors becomes the first priority.

Zirconium alloys possess a good combination of high corrosion resistance and neutron economy [3, 4], which makes them suitable for production of cladding tubes for water cooled reactors. One of the important aspects of cladding tubes is the great influence of fretting corrosion on the service behavior of these materials. Previous studies [5-7] have shown that fretting corrosion of cladding tubes was caused by flow induced vibration (FIV) and now has become the main reasons for the failure of fuel assembly. According to the global survey carried out by International Atomic Energy Agency (IAEA) [8], 57.9% of failures of cladding tubes originate from fretting corrosion in the year of 2011 to 2015, which brings great threat to the safe operation of the nuclear reactors.

Fretting corrosion happens on the contact surface of the wear couples, so the contact surface structure and properties determine the fretting corrosion resistance [9, 10]. Developing appropriate surface modification techniques to improve the resistance is a very promising approach. In fact, many surface modification treatments, such as vapor deposition, cold spraying and micro-arc oxidation, et al. [11-15] have been applied to improve the fretting corrosion resistance of zirconium alloys. Among them, shot peening, which is a fast and inexpensive way to form a hardened and nanocrystalline layer on the surface [16, 17], is also believed to be an effective way to improve the fretting corrosion resistance of zirconium alloy. The effects of shot peening on general corrosion and fretting wear behavior of different materials have been regularly studied. For example, Amouzouvi's work [18] indicates that the cold work and microstructure changes induced by shot peening increases the corrosion resistance of Zr-2.5Nb alloy in high temperature water. Fridrici [19] reported that for titanium alloys, shot peening has a beneficial effect on the crack initiation and propagation under fretting wear load. However, little work has been carried out on zirconium alloys serving in high temperature high pressure water (HTHPW).

The fretting wear behavior of various kinds of zirconium alloys without shot peening has been studied in other environments (air, low temperature water or HTHPW) [20-25]. Cai and Zhou [26] reviewed the research about fretting wear of zirconium alloys and concluded that the testing environment is one of the most important parameters determining the fretting wear behavior. For the tests carried out in water, Fisher [27] reported that under the impact fretting wear condition, the wear volume of zirconium alloy tested in water at temperatures below 150 ℃ is five to ten times larger than that in 250 ℃ - 286 ℃. Lazarevic and Qu's work [28] shows that the wear volume of zirconium alloy increases with the testing temperature of water increasing from 22 ℃ to 204 ℃. However, most of the research on fretting wear of zirconium alloys was carried out in air or low temperature water. This is because the experimental study of fretting wear of zirconium alloy in HTHPW is relatively more difficult to implement. In recent years, researchers in the nuclear field, including authors of this paper, have designed autoclave systems and test rigs to better study the fretting wear behavior of nuclear materials [9, 28] exposed to HTHPW. However, the tests on zirconium alloys exposed to HTHPW are still not enough in general, and the failure mechanism of the materials is not fully revealed.

The complication about the fretting corrosion mechanism is that it is synergically determined by the chemical corrosion and mechanical wear [29]. A formular has been developed to describe the coupling effects of chemical corrosion and mechanical wear on the fretting corrosion behavior, as shown bellows [30-33]:

$$W = M_0 + C_0 + \Delta W \quad (1)$$

where W is the whole wear volume of the materials, M_0 is the pure mechanical wear volume, C_0 is the pure (static) corrosion volume. ΔW is the synergic factor which consists of the mechanical-assisted corrosion factor (ΔC_M) and the corrosion-assisted mechanical wear factor (ΔM_C). Then formula (1) can be written as:

$$W = M_0 + C_0 + \Delta C_M + \Delta M_C \quad (2)$$

The synergic factor (ΔW) determines the fretting corrosion mechanism, but it is hard to be measured directly and precisely. This is because all the testing parameters, such as normal stress [34], sliding amplitude [35], water temperature and pH [36], can influence the synergic factor (ΔW). Most research about the fretting corrosion behavior of zirconium alloys focuses on the effects of those testing parameters on the wear volume/depth of the materials, while the coupling effects of chemical corrosion and mechanical wear on the failure process and mechanism have not been fully clarified, especially in HTHPW. In addition, surface modification brings more complication to the fretting corrosion process of zirconium alloys and makes this problem more difficult.

This paper aims at studying the fretting corrosion behavior of a zirconium alloy exposed to HTHPW, and clarifying the effects of shot peening. The fretted and unfretted surface of the zirconium alloys after fretting corrosion tests were carefully characterized by various advanced characterization techniques to reveal the failure mechanism of the materials.

2 Experimental procedure

2.1 Materials

The nominal composition of the as received zirconium tube specimen (external diameter of 9.5 mm and thickness of 0.65 mm) and shot peened zirconium tube specimen is Zr-0.5Sn-0.5Nb-0.3Fe. The microstructure of the as received specimen (ARS) is shown in Fig. 1(a). It can be found that equiaxed grains with average size ~1.5 μm exist in the materials. However, the surface of the ARS is polished, and obvious polished furrows are shown on the surface (as shown in Fig. 1(b)). The cross-sectional microstructure of the subsurface materials is shown in Fig. 1(c). It can be found that the subsurface grains are elongated along the polishing direction, and some grains are recrystallized.

Shot peening introduces changes to the surface morphology of the zirconium tube. The furrows originated from polishing disappear and obvious deformation signs appear on the surface, as shown in Fig. 1 (d). The cross-sectional microstructure of the subsurface materials in the shot peened specimen (SPS) is also different from that on ARS. Equiaxed grains with size of several nano-meters are formed on the subsurface materials. The residual stress in the SPS is measured by X-ray diffraction technique (XRD). The results show that compressive residual stress (in the direction parallel to the length of the specimen) exists in the shot peening affected zone, and the average value is ~340 MPa. The residual stress is not uniform in the shot peening affected zone, which is got by measuring 3 points at distances of 0 μm, 20μm and 50μm from the surface.

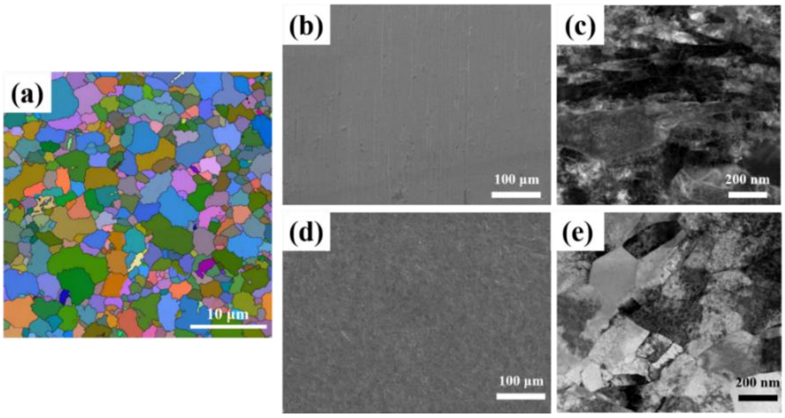

Fig. 1 (a) EBSD grain map showing the matrix microstructure of the ARS; SEM SE images showing the surface morphology of (b) ARS and (d) SPS; and TEM BF images showing the cross-sectional microstructure of subsurface materials of (c) ARS and (e) SPS

2.2 Fretting corrosion test

Fretting corrosion test was carried out in 300°C /15.5MPa distilled water with a tube-on-plate contact configuration, as schematically shown in Fig. 2(a). The fretting corrosion testing device has already been reported in a previous article [37]. The fretting corrosion testing parameters are listed as following: sliding amplitude of 80 μm, normal force of 6 N, frequency of 5 Hz and testing time of 24 hours. The counter-body material is 304 stainless steel with a composition of 19 wt.% Cr, 10 wt.% Ni, 2 wt.% Mn, 1.0 wt.% Si, 0.045 wt.% P, 0.030 wt.% S, 0.08 wt.% C and Fe balance. For each kind of materials, 3 samples were tested. The hardness of the wear couples is tested by Nano-Indentation technique on an Agilent NanoIndenter G200.

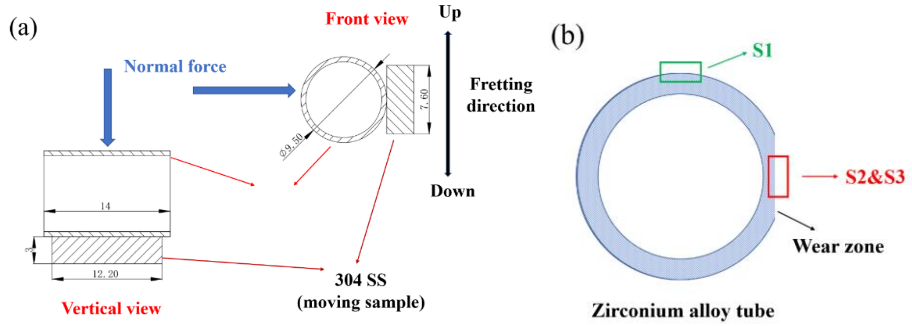

Fig. 2. (a) Schematic diagram of the contact mode between Zirconium alloy tube and the 304 stainless steel plate, (b) the sites where the TEM foils were extracted.

After the test, the wear volume of materials was measured by a 3D microscopy. For each kind of zirconium alloy specimen, one Transmission Electron Microscope (TEM) lift-outs (S1) were extracted from the unfretted surface by Focused Ion Beam (FIB), while two TEM lift-outs (S2 and S3) were extracted from the fretted surface, as schematically shown in Fig.2 (b). Then the morphology, element distribution, and phases of the cross-sectional surface (fretted and unfretted) oxide were characterized by Scanning Electron Microscope (SEM) and Electron Backscattered Diffraction (EBSD). High-resolution Transmission Kikuchi Diffraction (TKD) and Analytical TEM (ATEM) analyses were carried out on the TEM foils, respectively.

3 Results and discussion

3.1 Wear volume and wear surface analysis

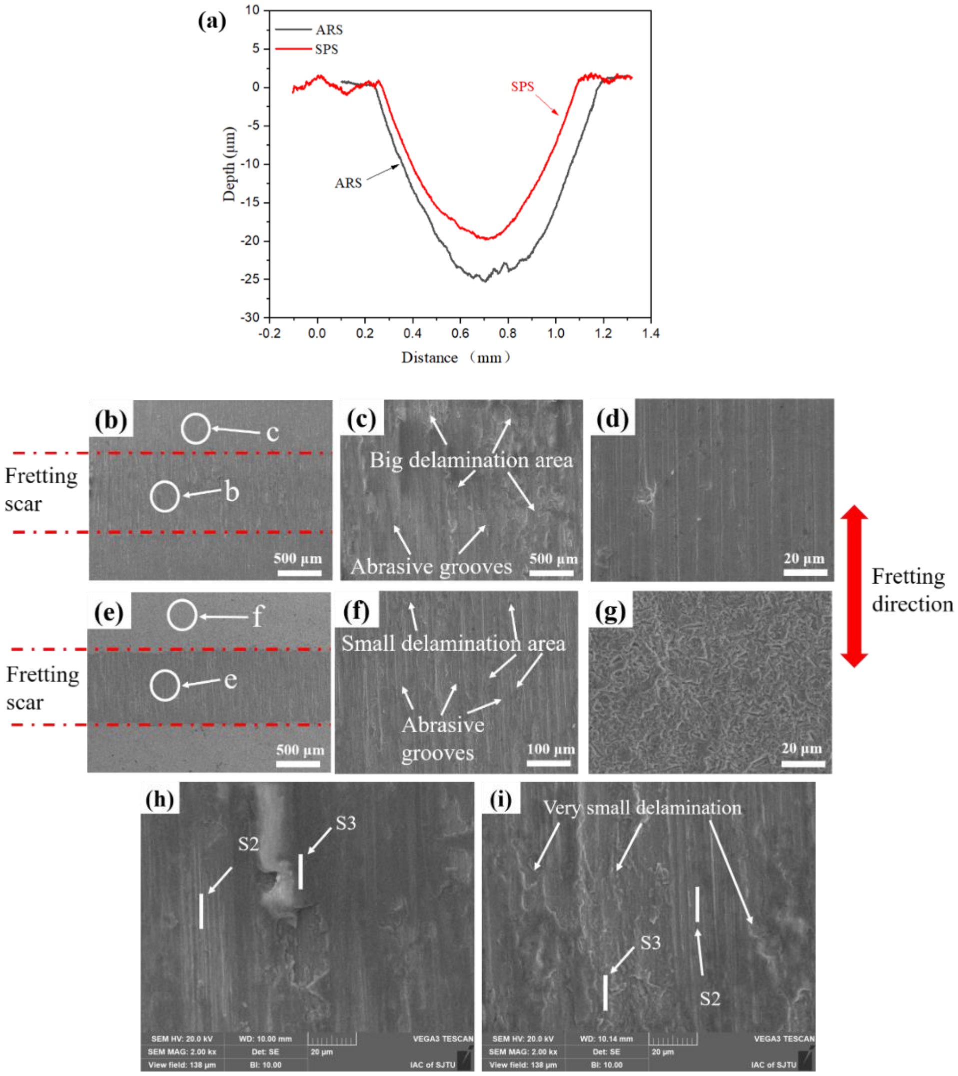

Fig. 3 (a) Cross-sectional profile of the wear scars; SEM SE images showing the surface morphology of (b) ARS and (c) SPS after test, magnified image of fretted surface of (c) ARS and (f) SPS, magnified image of unfretted surface of (d) ARS and (g) SPS; the location of the TEM foils extracted from the fretted surface of (h) ARS and (i) SPS

Based on the 3D microscopy analysis results, the cross-sectional profile of the wear scar is shown in Fig. 3 (a). Three specimens were tested in this study, and the average value of the wear volume and maximum wear depth for those three specimens are listed in Table 1. The wear volume of ARS is about 1.5 times of that of the SPS. The maximum wear depth of ARS is 25.2 μm, which is also higher than that of the SPS (19.8 μm). This indicates that shot peening increases the wear resistance of the zirconium alloy exposed to HTHPW greatly. A simple explanation is that the wear resistance of the materials is closely related to the surface hardness [38, 39], and higher hardness results in higher wear resistance of the materials. The surface micro-hardness of the specimens is also shown in Table 1. Shot peening increases the surface hardness of the zirconium alloy from 3.31 GPa to 4.55 GPa, and this could explain why the wear resistance of SPS is higher than that of ARS. It is necessary to point out that when nano indentation is used to measure the surface hardness, the indentation depth is ~360 nm and 280 nm for the ARS and SPS, respectively. However, for ARS, the surface polishing contributes to the formation of a deformation zone with thickness of~ 1.5 μm (shown in Fig. 4). For SPS, the thickness of the shot peening affected zone is ~300 μm. This indicates that the surface hardness measured does not represent the harness of the matrix alloy of ARS, which is expected to be much lower.

Table 1 Average wear volume, maximum wear depth and surface micro-hardness (tested by nano-indentation) of the materials

Specimens	**Wear volume (μm^3)**	**Maximum wear depth (μm)**	**Micro-hardness (GPa)**
ARS	(1.41±0.13) ×10^8	25.2±1.7	3.31±0.32
SPS	(7.56±0.89) ×10^7	19.8±1.2	4.73±0.54

The tests were carried out in HTHPW, which is a very corrosive environment and can influence the surface condition of the materials, specifically, the corrosive environment results in the oxidation of the fretting surface. Although shot peening increases the surface hardness by forming a dense and nano-sized grain layer on the surface (as shown in Fig.1 (d) and (e)), this layer can be altered by oxidation and wear in the fretting process, bringing complexity to this problem. The surface morphology and cross-sectional microstructure of the fretting surface needs to be characterized to clarify the failure mechanism.

Fig. 3 (b) and (e) shows that the width of the wear scar on ARS is bigger than that on SPS, which suggests that shot peening increases the wear resistance of the materials. The morphology of the fretted surface on ARS (Fig. 3(c)) and SPS (Fig. 3(f)) is not homogeneous: obvious characteristics of abrasive grooves are observed on the wear scar of both ARS and SPS, however, big delamination area only appears on the fretted surface of ARS, and very small delamination area is observed on the SPS. This indicates that the wear mode of the two materials is different, and shot peening hinders delamination in the fretting process. No crack is observed on the worn surface of neither ARS nor SPS.

The morphologies of the unfretted surface for the two kinds of materials are significantly different. Obvious machining marks are observed on the unfretted surface of ARS, as shown in Fig. 3 (d). This is because that the duration of the fretting test is only 24h, and the corrosion of the materials is at the initial stage, so a thin oxide scale is formed on the surface and the furrows originating from polishing are not fully covered. For the SPS, the unfretted surface is completely covered by the oxide scale, as shown in Fig. 3 (g).

The above observation indicates that for zirconium alloy, surface oxidation happens very fast in HTHPW. The oxide scale changes the surface condition of the materials, and this is crucial for determining the fretting wear behavior. In addition, it has been widely accepted that fretting wear also influences the oxidation/corrosion behavior of the fretted surface greatly [40, 41], which in turn determines the fretting wear behavior of the materials

3.2 Comparison of microstructure between the unfretted and fretted surface

To systematically evaluate the microstructure evolution of the zirconium alloy in the fretting corrosion process and reveal the coupling effects of corrosion and mechanical wear on the failure process, the cross-sectional microstructure of the unfretted and fretted surface needs to be analyzed and compared. The surface morphologies shown in Fig. 3 (b) and (c) / (e) and (f) indicate that the surface morphology after fretting test is not uniform: an abrasive area and a debris buildup area are both observed on the fretted surface. 2 TEM foils were extracted from the representative area with different morphologies, as shown in Fig. 3 (h) and (i). In addition, Fig. 3 (h) and (i) shows more clearly that a large delamination area is formed on the fretted surface of ARS, however, a small delamination area is formed on SPS.

3.2.1 Cross sectional microstructure of the unfretted surface

Fig. 4 shows the cross-sectional SEM-TKD analysis results of the unfretted surface on ARS. Clearly, after only 24 h exposure to simulated primary water, a very thin oxide layer with average thickness of ~200 nm is formed on the surface, which indicates that the oxidation of the zirconium alloy in high temperature water is very fast. Besides, a deformed metal layer with thickness of ~1.5 μm exists beneath the oxide layer, which originates from the surface machining process, and this is consistent with the results shown in Fig. 1 (c) that surface polishing results in the deformation of the surface grains, which are elongated and recrystallized in the polishing process. For zirconium alloy, the oxide layer is nanocrystalline, and initially equiaxed, then growing into columnar grains. In the early stage of oxidation, the oxide scale is composed of grains that are predominantly tetragonal (t-ZrO_2) [42-44].

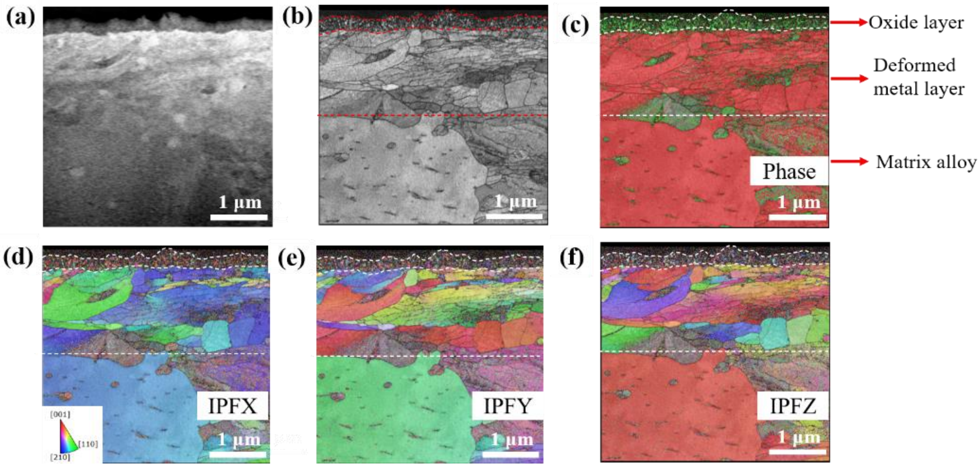

Fig. 4 Cross-sectional SEM-TKD analysis results of the unfretted surface on ARS (a) SEM image, (b) pattern quality map, (c) phase map and (d-f) IPF maps

The cross-sectional microstructure of the unfretted surface on SPS is also characterized, as shown in Fig. 5. It can be found that the surface of zirconium tube after shot peening is rough, as clearly indicated by the wave-shaped oxide scale in Fig. 5 (a). A continuous oxide scale with average thickness ~ 200 nm is also formed on the unfretted surface of SPS, which is similar to that formed on ARS.

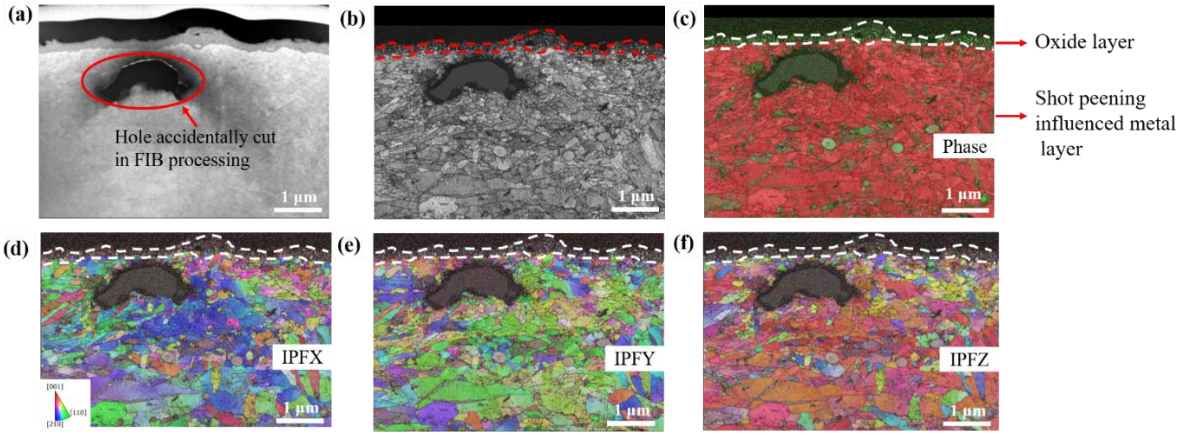

Fig. 5 Cross-sectional SEM-TKD analysis results of the unfretted surface on SPS (a) SEM image, (b) pattern quality map, (c) phase map and (d-f) IPF maps

The matrix microstructure in the SPS is very ununiform, and the closer the grains to the surface, the smaller the grain size. This is because that shot peening treatment can induce severe plastic deformation and this contributes to the refinement of the grains [16, 17]. In general, the grains near the surface are equiaxed and nano-sized. Although the surface morphologies (Fig. 3 (d) and (g)) show that the general corrosion behavior of the ARS and SPS is different, the thickness of the oxide scale is similar, which indicates that shot peening has little effects on the general corrosion behavior of the materials. The reason for this will be discussed in detail in next sections.

3.2.2 Microstructure evolution of the fretted surface on ARS

Fig. 6 and Fig. 7 shows the cross-sectional microstructure of the different areas (S2 and S3) on the fretted surface of ARS.

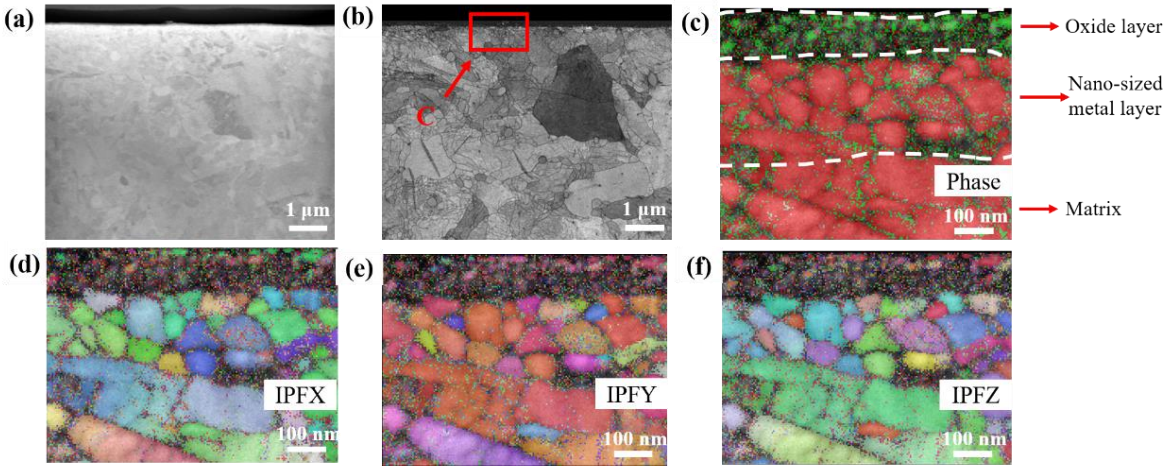

Fig. 6 Cross-sectional SEM-TKD analysis results of the S2 area on the fretted surface of ARS (a) SEM image, (b) pattern quality map, (c) phase map and (d-f) IPF maps

As shown in Fig. 6, a continuous oxide scale with average thickness of ~120 nm is formed on S2 area, which is thinner than the oxide scale formed on the unfretted surface (~200 nm). The maximum wear depth of the wear scar is 18.44 μm, which is much higher than the thickness of the deformed metal layer originating from the polishing treatment (~1.5 μm, as shown in Fig. 4). This indicates that the deformed metal layer has already been worn away in the fretting wear process. However, the TKD analysis results still show that a metal layer with nano-sized grains is formed beneath the oxide scale. This layer is different from the deformed layer on the ARS. The original grain size of matrix alloy is ~ 1.5 μm (Fig.1 (a)), which is much bigger than the recrystallized grains in the metal layer beneath the oxide layer. This indicates that recrystallization happens in matrix alloy beneath the oxide scale. This can be attributed to two reasons: firstly, the frictional movement in the fretting wear process results in the increment of the temperature on the surface [45], which is the driving force for recrystallization. Secondly, the matrix alloy is deformed in the fretting wear process, which contributes to the recrystallization of the matrix alloy.

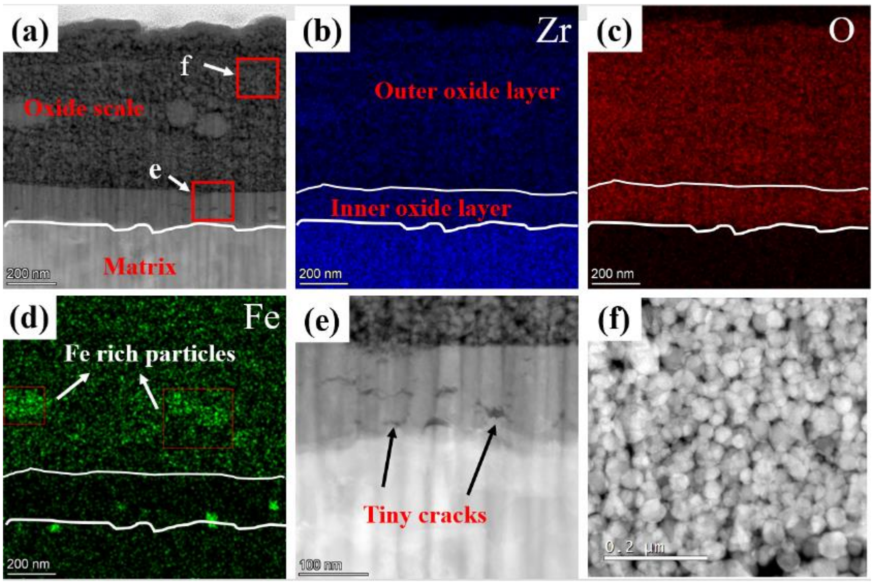

Fig. 7 Cross-sectional STEM analysis results of the S3 area on the fretted surface of ARS (a) STEM BF image, (b) to (d) EDS elemental mapping results, (e) and (f) STEM HAADF magnified images from regions labeled in (a)

After characterizing the S3 area, a totally different subsurface microstructure is observed, as shown in Fig. 7. An obvious oxide scale with average thickness of ~ 800 nm is formed on the fretted surface, which contains two layers. The outer layer has an average thickness of ~700 nm and is composed of discrete oxide particles (Fig. 7 (f)). The inner layer has an average thickness of ~100 nm, is compact, and also pressents small pores and cracks (Fig. 7 (e)). The EDS analysis results indicate that the composition of the two layers is different: the two layers are both rich in Zr and O, however, Fe enrichment is only observed in the outer layer. In addition, particles with high content of Fe are also observed in the outer layer.

In the fretting or sliding contact mode, the two contacting surfaces (in this study, zirconium alloy and 304 SS) are referred to as “first bodies”, while the particles that develops between the first bodies are called “third bodies” [46]. The “third bodies” (particles) are rolled and grinded in the fretting process, which can form a third body layer (TBL) on the fretted surface. In this study, it is obvious that the outer oxide layer is composed of the worn debris from the two counter bodies, which are oxidized in the fretting wear process. This layer is also porous and some Fe enrichment is observed in it.

The morphology, structure and composition of the inner oxide layer is different from the outer oxide layer. The outer oxide layer is porous, so HTHPW can reach the matrix easily, then the reaction between Zr and water happens, and a relatively compact inner oxide layer is formed beneath the outer oxide layer. Many tiny cracks are observed in the inner oxide layer. The formation mechanism for those cracks will be discussed in the following sections.

3.2.3 Microstructure evolution of the fretted surface on SPS

Fig. 8 and Fig. 9 shows the cross-sectional microstructure of the different areas (S2 and S3) on the fretted surface of SPS. Similar to the ARS specimen, a quite thin oxide layer with an average thickness of ~80 nm is formed on the S2 area, which is much thinner than that formed on the unfretted surface (~ 200nm, as shown in Fig. 5). In addition, it is also thinner than the oxide scale formed on the S2 area of ARS (~120 nm). Obvious nano-sized grains are observed in the metal materials beneath the oxide scale. Different from the results of ARS, the metal matrix beneath the oxide sale is fully recrystallized due to the shot peening treatment.

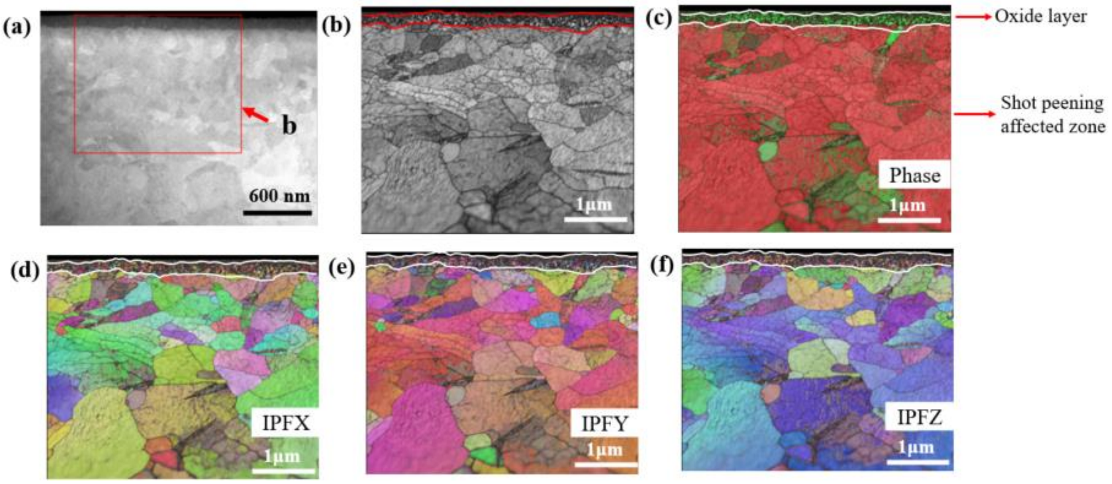

Fig. 8 Cross-sectional SEM-TKD analysis results of the S2 area on the fretted surface of SPS (a) SEM image, (b) pattern quality map, (c) phase map and (d-f) IPF map

The cross-sectional microstructure of the S3 area on SPS is shown in Fig. 9. It is obvious that a continuous oxide scale is also formed in this area. Like the oxide scale formed on the S3 area of ARS (shown in Fig. 7), a dual-layer structure oxide scale is also formed in this area. The composition of the oxide scale shown in Fig. 9 is not uniform, and relatively higher content of Fe is observed in the outer oxide layer. This is similar to that observed on ARS. The outer oxide layer is composed of oxide particles, while frequent big cracks (much bigger than that in the inner oxide layer of ARS) are distributed in the inner oxide layer.

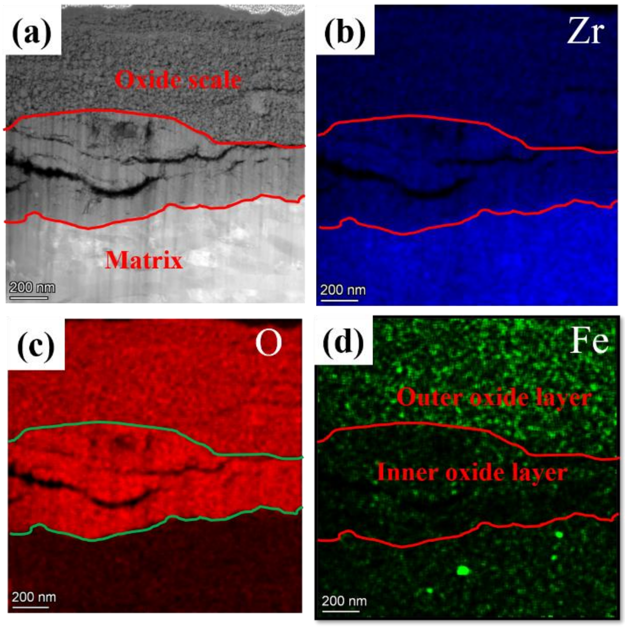

Fig. 9 Cross-sectional STEM analysis results of the S3 area on the fretted surface of SPS (a) STEM BF image, (b) to (d) EDS elemental mapping results

The average thickness of the inner oxide layer is ~ 450 nm, which is much thicker than that of the ARS. In addition, the microstructure of the inner layer on the two samples is quite different: more and larger cracks are formed in the inner oxide layer of SPS. The reasons for this will be discussed in the next section.

3.3 Failure mechanism of the materials

3.3.1 Wear mode analysis

The wear mode of the materials in HTHPW is changed after shot peening, as clearly shown by the surface morphology of the wear scar (Fig. 3). Delamination and abrasive wear happen simultaneously in the fretting wear process of ARS, however, for the SPS, abrasive wear is dominant, and only very small delamination area is observed. Delamination indicates that the oxide scale on the fretted surface is fragile, and can be broken, which contributes to the higher wear volume of the ARS.

According to the fretting maps theory [47], the fretting wear can be classified into stick regime, mixed stick-slip regime and gross slip regime, based on the state of interfacial contact. In general, the fretting regime is synergically controlled by the normal force and sliding amplitude. In this study, the normal force is only 6 N, and the sliding amplitude is 80 μm. The relatively low normal force and high sliding amplitude determines that the fretting is in the gross slip regime [24]. In this regime, the obvious materials response is that adhesion junction is completely eliminated from the contact surface and sliding wear takes place. Previous studies [48, 49] also found that delamination happens in the gross slip regime, and this is because the exhaustion of the ductility of the contacting materials through repetitive accumulation of plastic strain.

The macrophotograph of the cross-sectional microstructure of the oxide scale on the fretted surface (S3 area) of ARS and SPS is shown in Fig. 10 (a) and (b). It can be clearly seen that for the ARS, the cracks are long and parallel to the fretting direction, however, for the SPS, the cracks that parallel to the fretting direction is short. Most importantly, cracks perpendicular to the fretting direction are widely distributed on the oxide scale of SPS. Large delamination areas can be formed when the long cracks in the ARS propagate to the surface. While, for SPS, the cracks perpendicular to fretting direction contribute to the formation of a small delamination area in this condition

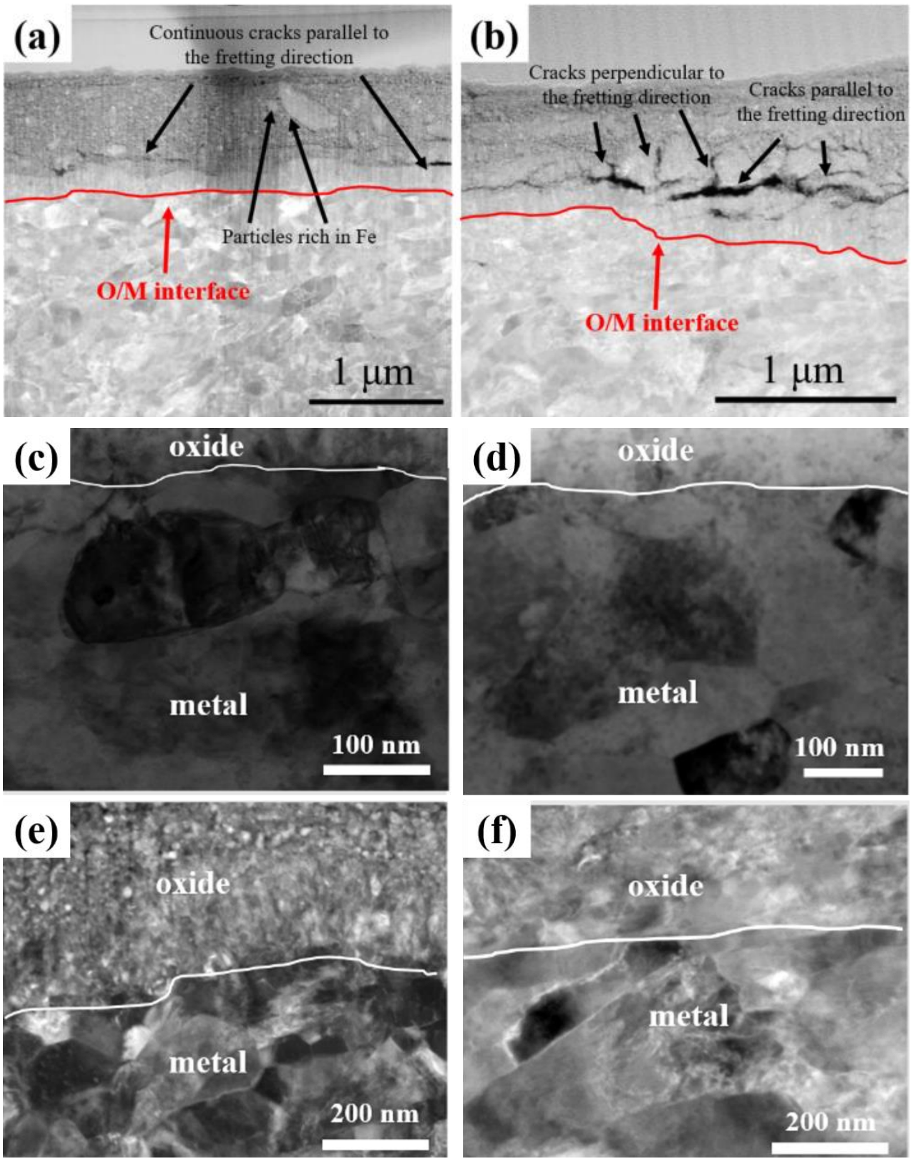

Fig. 10 Macrophotograph of the cross-sectional microstructure of the fretted surface (S3 area) on (a) ARS and (b) SPS; TEM BF images of the oxide/metal interface on the fretted surface of (c) ARS-S2, (d) SPS-S2, (e) ARS-S3, (f) SPS-S3

To further confirm the wear mode, the oxide/metal interface of fretted surface on the ARS and SPS is carefully examined by TEM and the results are shown in Fig. 10 (c) to (f). No cracks are observed at the oxide/metal interface of neither ARS nor SPS, regardless of the S2 or S3 area. For both kinds of materials, fine metal grains are formed beneath the oxide scale, and no pores or cracks are observed in this area. This indicates that the O/M interface and the metal matrix beneath it are not susceptible to crack initiation in the fretting wear process. Delamination only seems to occur in the oxide scale.

Materials transfer is believed to be an important mechanism [50, 51] for controlling the composition of the oxide scale formed on the fretting surface. In this study, the cross-sectional element analysis results shown in Fig. 7 and 9 indicate that Fe only present in the outer oxide layer of the debris build up area, however, the inner oxide layer is depleted of Fe, regardless of the ARS or SPS. In the fretting test, the counting material is 304 SS, and the Fe element is transferred from it to the fretted surface of zirconium alloy. The materials from 304 SS and the materials from zirconium tube are mixed due to the mechanical alloying in the fretting wear process, subsequently refined and oxidized to form the porous outer oxide layer. The inner oxide layer is formed by the reaction between Zr and HTHPW, so Fe does not exist in this layer.

3.3.2 General corrosion mechanism analysis

The fretting wear tests were carried out in HTHPW, which is very corrosive, so mechanical wear and chemical corrosion of the contact surface happen simultaneously in this process, which finally determines the failure mechanism of the material.

To analyze the corrosion behavior of the materials, the composition of the oxide scale needs to be studied. EELS is used to study the composition of the thin oxide scales, and the results are shown in Fig. 11.

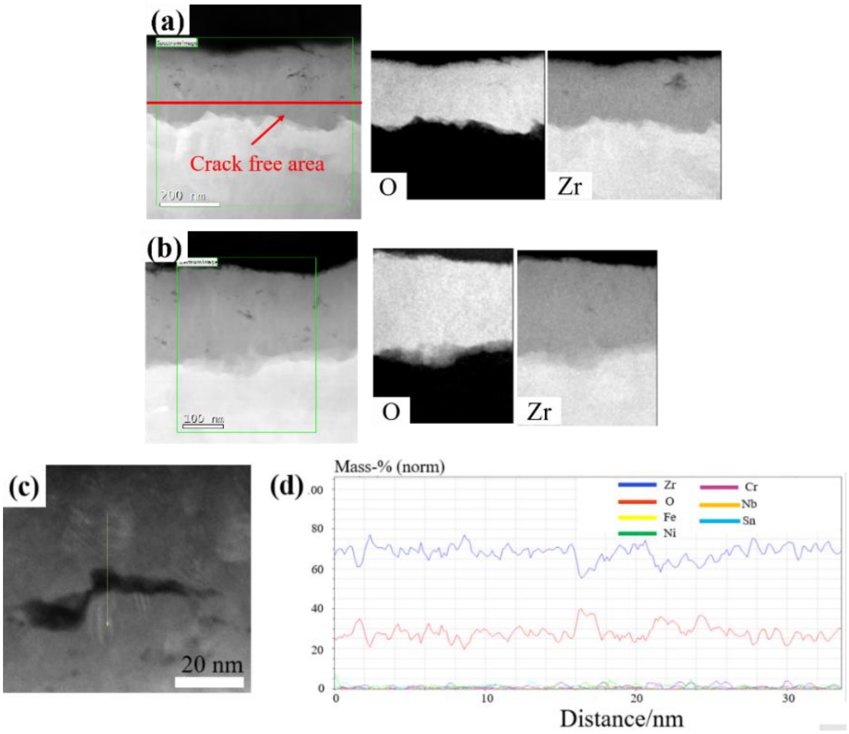

Fig. 11 Cross-sectional STEM HAADF image and EELS analysis results of the (a) unfretted surface on ARS, (b) unfretted surface on SPS; (c) High magnification image of representative black dots and (d) corresponding EDS line scanning results of the yellow line labeled in (c)

A continuous zirconium oxide scale is formed on the unfretted surface, which is mainly composed of Zr and O, with a composition matching ZrO_2, regardless of the ARS or SPS. Another obvious phenomenon is that for both ARS and SPS, many small black dots are observed in the oxide scale of the unfretted surface. To confirm what the black dots are, a higher magnification TEM image and EDS were used to characterize one of them, as shown in Fig. 11 (c). The results were consistent with them being a crack, instead of a second phase particle (SPP) or other substance.

The above characterization work shown in Fig. 11 further confirms that shot peening has a limited effects on the thickness, composition and structure of oxide scale on the unfretted surface of ARS and SPS, which is greatly different from previous research results showing that shot peening increases the corrosion resistance of many kinds of materials, such as zirconium alloy [52], titanium alloy [53] and stainless steels [54]. The main reason for the increment of corrosion resistance after shot peening treatment is that severe plastic deformation happens in this process, which brings high density dislocation and even grain recrystallization to the materials. Dislocations and grain boundaries are short-circuit diffusion paths for the inner diffusion of oxidizing species and this promotes the fast formation of a protective oxide scale, so the corrosion resistance of the materials after shot peening is increased.

However, a nano-sized grain layer with high dislocation density is also formed in the subsurface of ARS. This is because the surface of ARS is machined, which can also result in plastic deformation and grain refinement in the subsurface of the materials [55], depending on the machining parameters. Fig. 1 (c) and Fig. 4 show that a nano-size layer with thickness of ~1.5 μm is formed on the subsurface of ARS. The ARS and SPS specimens were tested in HTHPW for only 24h, so the general corrosion behavior is only determined by the thin nano-sized subsurface layer, and this is likely to be the main reason why the general corrosion behavior of SPS is similar to the ARS.

3.3.3 Fretting corrosion mechanism analysis

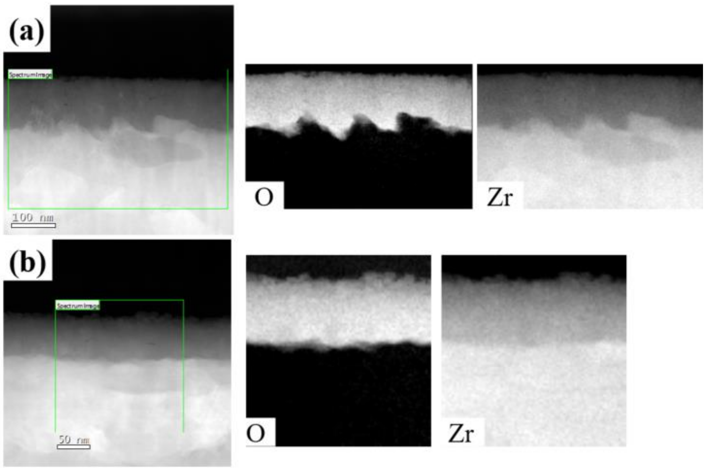

Fig. 12 Cross-sectional STEM HAADF image and EELS analysis results of the (a) fretted surface (S2 area) on ARS, (b) fretted surface (S2 area) on SPS

EELS is also used to study the composition of the thin oxide scale on the S2 area of the fretted surface, as shown in Fig. 12. The oxide scale is also only composed of Zr and O, matching ZrO_2, which is the same as the unfretted surface shown in Fig. 11. Fe is observed in the oxide scale of S3 area on the fretted surface, as shown in Fig. 7 and Fig. 9, which is different from the S2 area. This is because no “third body layer” (TBL, the outer oxide layer) exists in this abrasive area (S2 area), and the oxide scale is formed due to the direct reaction between Zr and HTHPW. The surface oxide scale is worn away directly since there is no TBL protecting it, resulting on the formation of a straight surface, as clearly shown in Fig. 12.

Compared with the oxide scale on the unfretted surface, there are fewer black dots appearing in the oxide scale of the fretted surface (S2 area). Moreover, the size of the black dots on the oxide scale of the fretted surface (S2 area) is much smaller. While in the inner layer of the oxide scale on the S3 area, several cracks are observed, as clearly shown in Fig. 7 and Fig. 9. In particular, for the SPS, the cracks in the inner oxide layer are much larger and longer than in the ARS.

The above discussion indicates that the corrosion behavior of the fretted surface on both ARS and SPS is changed by the mechanical wear. Unfortunately, the widely accepted fretting corrosion theory [30-32] listed in the Part 1 cannot be used to calculate the wear volume of the materials in this study. This is because the “corrosion” of metals in low temperature solution is related to the dissolution of the metallic elements, which results in the loss of material. However, the dissolution of Zr in high temperature high pressure water is neglectable so, in this study, the “corrosion” of the materials means the reaction between Zr and water (oxidation of the materials), and this ultimately results in the formation of zirconium oxide scale.

The classic fretting corrosion theory [30-32] still gives a clear definition that the coupling effects of mechanical wear and chemical corrosion determine the fretting corrosion behavior of materials. By comparing the microstructure, composition, and thickness of the oxide scale on the fretted and unfretted surface, obvious mechanical-assisted corrosion (oxidation in this study) is observed, which can be summarized as following:

(1) Formation of thick porous outer oxide layer on the debris buildup area (S3). The flakes delaminated from the wear couples are easily grinded and oxidized in the fretting movement, which accumulate and form the porous outer oxide layer.

(2) The porous outer oxide layer can not hinder the direct contact between the matrix alloy and the water, so the matrix alloy is not protected, and the corrosion (oxidation) of the metal continues, which results in the formation of an inner oxide layer with similar thickness to the oxide scale of the unfretted surface.

(3) Loss of protective oxide scale on the abrasive area (S2). The thickness of the oxide scale in this area is ~ 80 nm, which is much thinner than that on the unfretted area (~ 200nm). This indicates that the oxide scale is worn away in this area. Once the oxide scale is fully damaged, the corrosion (oxidation) of the materials is accelerated.

In general, the mechanical wear promotes the corrosion (oxidation) of the zirconium alloy. As for the corrosion-assisted mechanical wear, the following conclusions can be summarized:

(1) Oxide scale is formed on the fretted surface, regardless of the abrasive area

(S2 area) or debris buildup area (S3 area). The hardness of the oxide scale is much higher than the matrix alloy [56], so the mechanical wear is relieved due to the good wear resistance of the oxide scale.

(2) Delamination happens on the fretted surface (S3 area), as a consequence of the oxide scale undergoing cyclic frictional stresses in the fretting wear process, which results in the formation of cracks in the oxide scale.

(3) Once delamination happens, the wear rate of the materials is accelerated. In addition, the flakes originating from the delamination of the materials can become wear particles, which further promote abrasive wear of the materials.

So in this study, it is hard to conclude that oxidation of the zirconium alloy is beneficial to the increment of the wear resistance.

3.3.4 Crack formation mechanism analysis

The formation of cracks in the oxide scale on the fretted surface is a key issue that determines if delamination happens. The theoretical explanation for delamination [10, 57, 58] is that the dislocations pile up under the fretted surface, which leads to void coalescence and cracks parallel to the surface form. In the propagation process, the crack can shear to the surface when a weak position is reached, which results in the formation of thin wear sheets.

It is also known that cracks can appear in zirconium alloys as a consequence of corrosion. In particular, larger longitudinal cracks parallel to the oxide metal interface are expected after the so-called “transitions” in the oxidation rate [59, 60]. Smaller ones, such as those observed in Fig. 11, are more typical of pre-transition oxidation regimes. This will be explained in more detail in the next section.

(1) Cracks formed in the oxide scale on the unfretted surface

For the general corrosion process of zirconium alloy, Kirkendall effect (ions of alloying elements, such as Fe^{3+}, diffuse faster in ZrO_2 than Zr^{4+}) results in the formation of pores or small cracks in the oxide scale [61-63]. In addition, high compressive stress appear in the zirconium oxide scale due to the high Pilling-Bedworth ratio of ZrO_2/Zr couple, and the value of the compressive stress at the initial stage can be as high as 1500 MPa [64, 65]. The value of the compressive stress is highest at the O/M interface, and gradually decreases with the distance from the O/M interface. The compressive stress stabilizes the tetragonal ZrO_2 (t-ZrO_2), which transforms to monoclinic phase (m-ZrO_2) when the compressive stress decreases to a critical value [66, 67]. The transformation of the oxide phase results in the formation of micro-pores and small cracks in the oxide scale. The above two mechanisms work simultaneously and the cracks are formed in the oxide scale on the unfretted surface.

As shown in Fig. 11, the thickness and composition of the oxide scale on the unfretted surface of ARS and SPS is similar. However, the crack distribution in the two kinds of materials is greatly different. For ARS, the cracks are distributed far away from the O/M interface. This phenomenon is normal, as explained by the above discussion that the compressive stress is decreasing with the increase of the distance from the O/M interface. The crack distribution in the oxide scale of the SPS is homogeneous, and many cracks are observed in the area near the O/M interface. This is different from that in the ARS and previous studies [61-63]. The reason for this is discussed next.

(2) Cracks formed in the oxide scale on the fretted surface

For the fretting corrosion process of zirconium alloy, two different crack formation behaviors are observed on the fretted surface:

(1) On the abrasive area (S2 area), a thin oxide scale with average thickness of ~80 nm is present , which indicates that the oxidation of the materials still happens in the fretting wear process, so the cracks can still be formed because of the Kirkendall effect and the transformation of t-ZrO_2 to m-ZrO_2 [62-64]. However, severe material loss happens due to the abrasive wear [68] and the oxide scale is quickly worn away, so the cracks are hardly observed in the oxide scale on this area.

(2) On the debris buildup area (S3 area), a thick oxide scale with dual layer structure is formed. However, the size and distribution of cracks for ARS and SPS are different:

(a) For ARS, large size cracks parallel to the fretting direction are widely distributed in the porous outer oxide layer. Very small cracks are formed in the inner oxide layer, and the average thickness of the inner oxide layer is ~200 nm, which is similar to that of the unfretted surface.

(b) For SPS, the outer oxide scale in this area is also porous and cracks are distributed in it. However, a relatively high density of large cracks exist in the inner oxide layer. In addition, the orientation of the cracks is diverse: besides cracks parallel to the fretting direction, cracks perpendicular to the fretting direction are also observed.

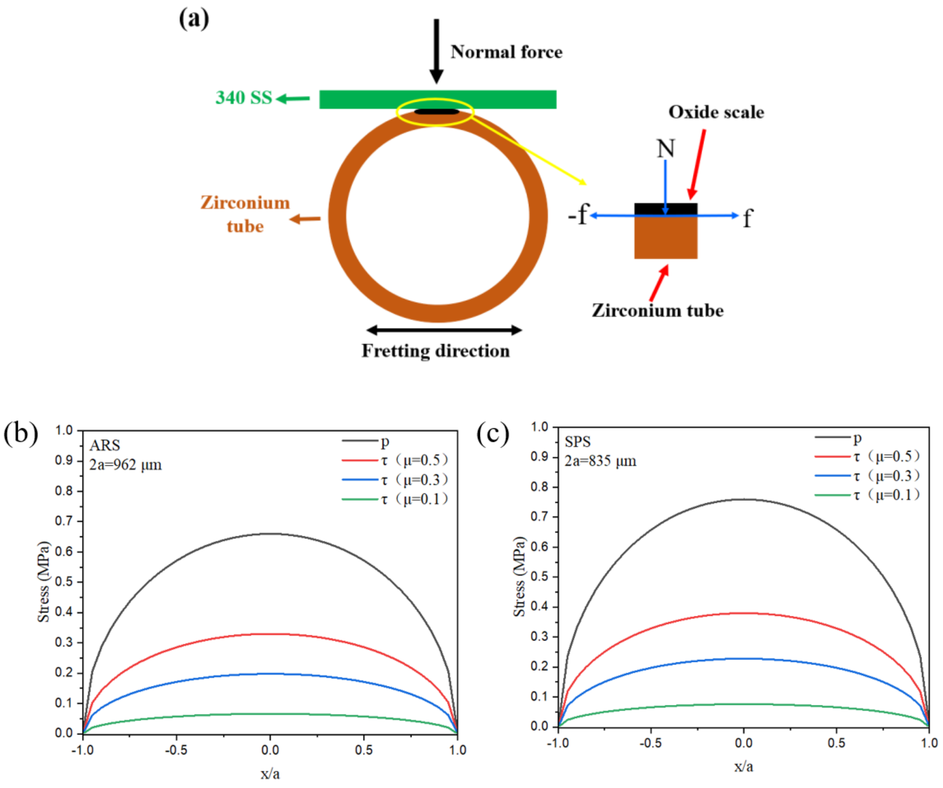

Fig. 13 (a) Schematic picture showing the contact between a cylindrical body and a plate; (b)

the normal pressure and (c) cyclic frictional stress acting on the fretting surface of ARS and SPS

The cyclic tangential stress acting on the zirconium alloy is the key parameter that determines the crack initiation and growth behavior. The stress status of the contacting surface is schematically shown in Fig. 13 (a). According to the classic Hertz's theory, the normal pressure (parallel to the z axial direction) acting on the surface of zirconium alloy can be expressed by the following equation:

$$p(x) = -p_0(1 - \frac{x^2}{a^2})^{1/2} \tag{3}$$

where x is distance from the original point schematically shown in Fig. 13 (a), a is the half length of the contacting area in the x axial, p_0 is the maximum pressure and can be given by

$$p_0 = (\frac{FE^*}{\pi LR})^{1/2} \tag{4}$$

where F is the load acting on the specimen, L is the length of the cylindrical body, R is the radius of the cylindrical body, E^* is the equivalent elastic modulus of two contact bodies, and can be given by

$$\frac{1}{E^*} = \frac{1-v_1^2}{E_1} + \frac{1-v_2^2}{E_2} \tag{5}$$

where v_1 is the Poisson's ratio of the cylindrical body, E_1 is the Young's modulus of the cylindrical body, v_2 is the Poisson's ratio of the plate, E_2 is the Young's modulus of the plate.

In fact, the elastic modulus of two contact bodies is changed with the formation of oxide on the surface, which means that equation (3) can't be used to accurately calculate p(x). In addition, the value of a is not a fixed value in the fretting wear process, which is always changing. If the value of a is fixed, the normal pressure can be calculated by the following equation:

$$p_0 = \frac{2F}{\pi La} \tag{6}$$

Then the cyclic frictional stress f (parallel to the x axial direction) acting on the contacting surface can be calculated by the following equation:

$$\mathrm{f(x)} = \mu p(x) = \mu p_0(1 - \frac{x^2}{a^2})^{1/2} \tag{7}$$

where μ is the friction coefficient.

By using equation (3), (6) and (7), p(x) and f(x) are calculated with the parameters listed in Table 2, and the results are shown in Fig. 13 (b) and (c). The wear coefficient is unknown and cannot be measured in HTHPW, so it is set to be 0.1, 0.3 and 0.5.

Table 2 Parameters used for the calculation of the contact pressure and cyclic frictional stress for ARS and SPS

Parameters	ARS	SPS
μ	0.1~0.5	0.1~0.5
N	6 N	6 N
2a	962 μm	835 μm
L	12 mm	12 mm

The results show that the maximum pressure acting on the fretting surface of ARS is ~0.66 MPa, while for SPS, the value is ~ 0.76 MPa. The value of cyclic frictional stress acting on the fretting surface of ARS is calculated to be in the range of 0.066MPa to 0.33 MPa. While for SPS, the value is calculated to be in the range of 0.076MPa to 0.38MPa. The difference between the cyclic frictional stress is very small for ARS and SPS. It is necessary to point out that the calculated normal stress and cyclic frictional stress shown in Fig. 18 reflects the ideal status that the surface of the wear couples is flat and the contact between the wear couples is uniform. In this condition, the contact load is only sufficient to cause tiny elastic deformation at the macroscopic level.

However, the surface of the wear couples is rough, as clearly shown in Fig. 3. According to the work of Greenwood [69], the ratio between the actual contact area (A_C) and the nominal contact area (A_0) (A_C / A_0) can be as low as 0.01. Suppose the value of A_C / A_0 is 0.01, then the cyclic frictional stress acting on the fretting surface of ARS is calculated to be in the range of 6.6 MPa to 33 MPa. While for SPS, the value is calculated to be in the range of 7.6 MPa to 38 MPa. Previous research [70, 71] show that the fatigue strength of zirconium alloys with similar composition at 350 °C is over 100 MPa, which is much higher than the cyclic frictional stress (lower than 40 MPa) calculated. So, cracks cannot be formed in the matrix alloy if the cyclic frictional stress acting on the materials is as calculated.

The magnified image of the outer oxide layer shown in Fig. 7 (f) clearly indicates that there are pores between the oxide particles. Those pores are easily to be linked together to form cracks in the fretting process. So, cracks are widely formed in the outer oxide layer of the oxide scale on the debris buildup area, regardless of the ARS or SPS.

Another obvious difference between the fretting corrosion behavior of ARS and SPS is that the size and amounts of cracks in the inner oxide layer of the debris buildup area (S3) are different, as shown in Fig. 7 and 9. The cyclic frictional stress or normal stress acting on the fretting surface is too small to initiate cracks in the materials, so the internal stress is the only reason for the formation of cracks in the inner layer of the oxide scale.

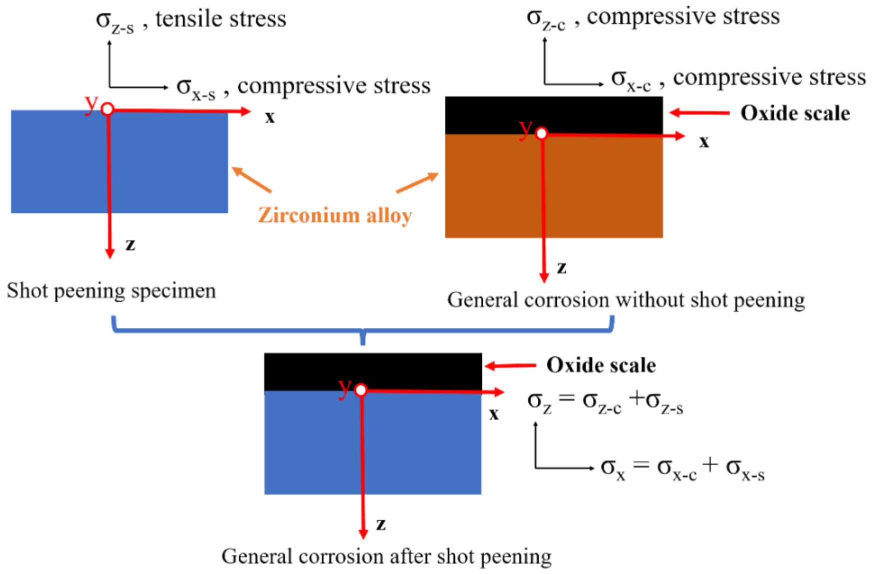

Fig. 14 Internal stress status of the inner layer in the oxide scale

The internal stress status of ARS and SPS in the corrosion process is schematically shown in Fig. 14. Shot peening not only brings in plastic deformation and grain refinement to the matrix alloy, but also introduces high residual stress. The residual stress along the x direction ($\sigma_{x\text{-}s}$) is compressive, as schematically shown in Fig. 14, with a value measured to be ~ 354MPa. The residual stress along the z direction ($\sigma_{z\text{-}s}$) is tensile. In the general corrosion process, compressive stress is also formed in the oxide scale due to the high Pilling-Bedworth ratio of ZrO_2/Zr couple [72], which is in the range of 0-500 MPa at the initial corrosion stage. In fact, the internal stress acting on the oxide scale along the z direction ($\sigma_{z\text{-}c}$) is smaller than that along the x direction ($\sigma_{x\text{-}c}$), since -z direction is the free direction (surface).

Considering the internal stress formed in the shot peening and corrosion process, the total principle shear stress τ_1 can be calculated by the following equation:

$$\tau_1 = \frac{1}{2}|\sigma_x - \sigma_z| = \frac{1}{2}|(\sigma_{x-c} + \sigma_{x-s}) - (\sigma_{z-c} + \sigma_{z-s})| \qquad (7)$$

Since the directions of $\sigma_{z\text{-}s}$ and $\sigma_{z\text{-}c}$ are opposed, the principle shear stress in the oxide scale of the materials with shot peening is bigger than that without shot peening, so more cracks are formed in the inner oxide layer. The higher principle shear stress resulting from shot peening contributes to the earlier cracking of the oxide scale, so cracks are formed near the O/M interface. This also explains the phenomenon shown in Fig. 11 that the cracks are distributed homogeneously in the oxide scale of the unfretted surface on SPS.

The more cracks in the inner oxide scale, the easier the cracks can shear to the surface, which is clearly observed in Fig. 10, where many cracks perpendicular to the fretting direction are formed in SPS. When those cracks propagate to the interface of outer oxide layer and inner oxide layer, they can connect with the pores and cracks in the outer oxide scale shown in Fig. 7 (f), then the delamination happens and this results in the formation of small delamination area, as shown in Fig. 3. The small flakes delaminated from the surface are more easily to be worn into abrasive particles, which further promotes the abrasive wear of SPS.

4 Conclusions

Fretting corrosion tests are carried out on zirconium alloys exposed to HTHPW. The failure process and mechanism of the materials is revealed by advanced characterization techniques. The following conclusions are drawn:

(1) Shot peening increases the fretting wear resistance of zirconium alloys exposed to HTHPW. The wear volume of the materials is reduced by ~46% after shot peening.

(2) The wear mode of the as received specimen (ARS) is abrasive wear and delamination. However, for shot peened specimen (SPS), the wear mode is mainly abrasive wear.

(3) The general corrosion behavior of ARS and SPS is similar, which is attributed to the short corrosion time and similar subsurface microstructure of the two

kinds of materials.

(4) Mechanical wear promotes the formation of a dual-layer structure oxide scale and the worm away of oxide scale on the fretted surface, which accelerates the corrosion of materials. However, the effect of corrosion on mechanical wear of the materials is controversial, and depends on the structure of oxide scale.

(5) The cyclic frictional stress acting on the materials is so small that it can neither break the matrix nor the O/M interface. The internal stress originates from shot peening and general corrosion contributes to the formation of cracks in the inner oxide scale of the fretted surface.

(6) Shot peening contributes to the higher principle shear stress in the oxide scale, which contributes to the formation of cracks, regardless of the fretted or unfretted surface.

Acknowledgements

This work is financially supported by the National Research Program with granted number of 2018YFB1900405.

References

[1] Brook BW, Bradshaw CJA, Key role for nuclear energy in global biodiversity conservation, Conserv. Biol. 29 (2015) 702-712.

[2] Nuclear power in China report, Word Nuclear Associations (2021).

[3] Mikhail K, Aliev T, Likhanskii VV, The modeling of the hydrogen solid solubility hysteresis in zirconium alloys, Acta Mater. 177 (2019) 131-140.

[4] Guerain M, Duriez C, Grosseau-Poussard JL, Mermoux M, Review of stress fields in Zirconium alloys corrosion scales, Corros. Sci. 95 (2015) 11-21.

[5] Kim KT, The study on grid-to-rod fretting wear models for PWR fuel, Nucl. Eng. Des. 239 (2009) 2820-2824.

[6] Wang H, Hu Z, Lu W, Thouless MD, The effect of coupled wear and creep during grid-to-rod fretting, Nucl. Eng. Des. 318 (2017) 163-173.

[7] Hu Z, Developments of analyses on grid-to-rod fretting problems in pressurized water reactors, Prog. Nucl. Energ. 106 (2018) 293-299.

[8] Vienna : International Atomic Energy Agency, 2019. Series: IAEA nuclear energy series, ISSN 1995-7807; No. NF-T-2.5.

[9] Lai P, Zhang H, Zhang L, Zeng Q, Lu J, Guo X, Effect of micro-arc oxidation on fretting wear behavior of zirconium alloy exposed to high temperature water, Wear 424-425 (2019) 53-61.

[10] Korres S, Feser T, Dienwiebel M, In situ observation of wear particle formation on lubricated sliding surfaces, Acta Mater. 60 (2012) 420-429.

[11] Slobodyan M, High-energy surface processing of zirconium alloys for fuel claddings of water-cooled nuclear reactors, Nucl. Eng. Des. 382 (2021) 111364.

[12] A AO, A GEF, A RB, B JT, The effect of Zircaloy-4 substrate surface condition on the adhesion strength and corrosion of SiC coatings, J. Nucl. Mater. 346 (2005)

109-119.
[13] Maier BR, Garcia-Diaz BL, Hauch B, Olson LC, Sindelar RL, Sridharan K, Cold spray deposition of Ti2AlC coatings for improved nuclear fuel cladding, J. Nucl. Mater. (2015) 712-717.
[14] Wang YM, Feng W, Xing YR, Ge YL, Guo LX, Ouyang JH, Jia DC, Zhou Y, Degradation and structure evolution in corrosive LiOH solution of microarc oxidation coated Zircaloy-4 alloy in silicate and phosphate electrolytes, Appl. Surf. Sci. 431 (2018) 2-12.
[15] Lorenzo-Martin C, Ajayi OO, Hartman K, Bhattacharya S, Yacout A, Effect of Al2O3 coating on fretting wear performance of Zr alloy, Wear 426-427 (2019) 219-227.
[16] Child DJ, West GD, Thomson RC, Assessment of surface hardening effects from shot peening on a Ni-based alloy using electron backscatter diffraction techniques, Acta Mater. 59 (2011) 4825-4834.
[17] B., Hashemi, And, M., Rezaee, Yazdi, And, V., Azar, The wear and corrosion resistance of shot peened–nitrided 316L austenitic stainless steel, Mater. Des. 32 (2011) 3287-3292.
[18] K.F. Amouzouvi, L.J. Clegg, R.C. Styles, J.E. Winegar, Effect of shot peening and post-peening heat treatments on the microstructure, the residual stresses and hardness, corrosion and deuterium uptake resistance of Zr-2.5Nb pressure tube material, WIT Trans. Eng. Sci. 2 (1993) 145-154.
[19] Fridrici V, Fouvry S, Kapsa P, Effect of shot peening on the fretting wear of Ti–6Al–4V, Wear 250 (2001) 642-649.
[20] Cho KH, Kim TH, Kim SS, Fretting wear characteristics of Zircaloy-4 tube, Wear 219 (1998) 3-7.
[21] Attia MH, On the fretting wear mechanism of Zr-alloys, Tribol. Int. 39 (2006) 1320-1326.
[22] Winter TC, Neu RW, Singh PM, Kolaya LE, Deo CS, Fretting wear comparison of cladding materials for reactor fuel cladding application, J. Nucl. Mater. 508 (2018) 505-515.
[23] Jiang H, Duan Z, Zhang BB, Zhao X, Wang P, Wear behavior of Zirconium-4 alloy after different irradiation damage level, Appl. Surf. Sci. 509 (2020) 145373.
[24] Yuan X, Zhang X, Zhang Q, Pu J, Zhu M, Study on the Fretting maps of Zircaloy-4 Alloy against Inconel 718 Alloy, Tribol. Int. (2021) 107024.
[25] Blau PJ, A microstructure-based wear model for grid-to-rod fretting of clad nuclear fuel rods, Wear 426-427 (2019) 750-759.
[26] Cai Z, Li Z, Yin M, Zhu M, Zhou Z, A review of fretting study on nuclear power equipment, Tribol. Int. 144 (2020) 106095.
[27] Fisher NJ, Weckwerth MK, Grandison D, Cotnam BM, Fretting-wear of zirconium alloys, Nucl. Eng. Des. 213 (2002) 79-90.
[28] Sladjan L, Lu RY, Cyrille F, George P, Blau PJ, Qu J, Investigating Grid-to-Rod Fretting Wear of Nuclear Fuel Claddings Using a Unique Autoclave Fretting Rig, Wear 412-413 (2018) 30-37.
[29] Wang W, Wang K, Zhang Z, Chen J, Cai W, Ultrahigh tribocorrosion resistance

of metals enabled by nano-layering, Acta Mater. 206 (2021) 116609.

[30] Iwabuchi A, Lee JW, Uchidate M, Synergistic effect of fretting wear and sliding wear of Co-alloy and Ti-alloy in Hanks' solution, Wear 263 (2007) 492-500.

[31] Stack MM, Mathew MT, Hodge C, Micro-abrasion–corrosion interactions of Ni–Cr/WC based coatings: Approaches to construction of tribo-corrosion maps for the abrasion–corrosion synergism, Electrochim. Acta. 56 (2011) 8249-8259.

[32] Wang Z, Huang W, Yan L, He H, Zhou Y, Zheng Z, Tribocorrosion behaviour of a biomedical Ti-25Nb-3Mo-3Zr-2Sn alloy in Ringer's solution, Mater. Sci. Eng., C 76 (2017) 1094.

[33] Rasool, G., Stack, M., M., Mridha, S., Mapping wear mechanisms of TiC/Ti composite coatings, Wear 328 (2015) 498-508.

[34] Mali SA, Zhu D, Liu Y, Gilbert JL, Fretting crevice corrosion of 316 L stainless steel in physiological phosphate buffered saline: Load, potential and alloy counterface effects, Tribol. Int. 164 (2021) 107198.

[35] Guo X, Lai P, Li L, Tang L, Zhang L, Progress in studying the fretting wear/corrosion of nuclear steam generator tubes, Ann. Nucl. Energy. 144 (2020) 107556.

[36] Royhman D, Pourzal R, Hall D, Lundberg HJ, Mathew MT, Fretting-corrosion in hip taper modular junctions: The influence of topography and pH levels – An in-vitro study, J. Mech. Behav. Biomed. 118 (2021) 104443.

[37] Guo X, Lai P, Tang L, Wang J, Zhang L, Effects of sliding amplitude and normal load on the fretting wear behavior of alloy 690 tube exposed to high temperature water, Tribol. Int. 116 (2017) 155-163.

[38] Wei S, Zhang H, Tangpatjaroen C, Tarnsangpradit J, Usta AD, Eriten M, Perepezko JH, Szlufarska I, Wear-induced microstructural evolution of ultra-fine grained (UFGs) aluminum, Acta Mater. 209 (2021) 116787.

[39] Reza G, Polycarpou AA, Three-body Abrasive Wear of Hard Coatings: Effects of Hardness and Roughness, Thin Solid Films. 666 (2018) S102522243.

[40] Majdouline Maher, Itziar Iraola-Arregui, Hicham Ben Youcef, Benaissa Rhouta, Vera Trabadelo. The synergistic effect of wear-corrosion in stainless steels: A review, Mater. Today: Proc. In press.

[41] Stott FH, Jordan MP, The effects of load and substrate hardness on the development and maintenance of wear-protective layers during sliding at elevated temperatures, Wear 250 (2001) 391-400.

[42] Qin W, Nam C, Li HL, Szpunar JA, Tetragonal phase stability in ZrO2 film formed on zirconium alloys and its effects on corrosion resistance, Acta Mater. 55 (2007) 1695-1701.

[43] Liu J, Yu H, Karamched P, Hu J, Grovenor C, Mechanism of the α-Zr to hexagonal-ZrO transformation and its impact on the corrosion performance of nuclear Zr Alloys, Acta Mater. 179 (2019) 328-341.

[44] J.P. Pemsler, The kinetics and mechanism of oxide film growth of Zirconium, Electro-chem. Technol. 4 (128) (1966).

[45] Lortz R, Junod A, Jaccard D, Wang Y, Meingast C, Masui T, Tajima S, Evolution of the specific-heat anomaly of the high-temperature superconductor YBa2Cu3O7

under influence of doping through application of pressure up to 10 GPa, J. Phys.-Condens. Mat. 17 (2005) 4135-4145.

[46] Rigney DA, Karthikeyan S, The Evolution of Tribomaterial During Sliding: A Brief Introduction, Tribol. Lett. 39 (2010) 3-7.

[47] Zhou ZR, Nakazawa K, Zhu MH, Maruyama N, Vincent L, Progress in fretting maps, Tribol. Int. 39 (2006) 1068-1073.

[48] Aica B, D F, Ftae F, Jg G, Highly porous Ti as a bone substitute: triboelectrochemical characterization of highly porous Ti against Ti alloy under fretting-corrosion conditions, Corros. Sci. 190 (2021) 109696.

[49] Xin L, Yang BB, Li J, Lu YH, Shoji T, Wear damage of Alloy 690TT in partial and gross slip fretting regimes at high temperature, Wear 390 (2017) 71-79.

[50] Singh K, Tiwari M, Mahato A, Evolution of regimes of wear in zircaloy-4/inconel-600 contact subjected to fretting loading, Tribol. Int. 147 (2020) 106274.

[51] Kirk AM, Sun W, Bennett CJ, Shipway PH, Interaction of displacement amplitude and frequency effects in fretting wear of a high strength steel: Impact on debris bed formation and subsurface damage, Wear 482-483 (2021) 203981.

[52] Mordyuk BN, Karasevskaya OP, Prokopenko GI, Khripta NI, Ultrafine-grained textured surface layer on Zr–1%Nb alloy produced by ultrasonic impact peening for enhanced corrosion resistance, Surf. Coat. Technol. 210 (2012) 54-61.

[53] Zhang Q, Duan B, Zhang Z, Wang J, Si C, Effect of ultrasonic shot peening on microstructure evolution and corrosion resistance of selective laser melted Ti-6Al-4V alloy, J. Mater. Res. Technol. 11 (2021) 801-804.

[54] Mahajan S, Sharma S, Goyal D, Chhibber R, Effect of shot peening on the high temperature molten salt corrosion resistance of P91 boiler steel, Mater. Today: Proc. 41 (2021) 801-804.

[55] Chang L, Burke MG, Scenini F, Understanding the effect of surface finish on stress corrosion crack initiation in warm-forged stainless steel 304L in high-temperature water, Scripta Mater. 164 (2019) 1-5.

[56] Li ZY, Cai ZB, Cui XJ, Liu RR, Zhu MH, Influence of nanoparticle additions on structure and fretting corrosion behavior of micro-arc oxidation coatings on zirconium alloy, Surf. Coat. Technol. 410 (2021) 126949.

[57] Mhaa B, Adpb C, Gw D, Effect of temperature on tribo-oxide formation and the fretting wear and friction behavior of zirconium and nickel-based alloys, Wear 476 (2021) 203722.

[58] Nagentrau M, Mohd Tobi AL, Jamian S, Otsuka Y, Hussin R, Delamination-fretting wear failure evaluation at HAp-Ti-6Al–4V interface of uncemented artificial hip implant, J. Mech. Behav. Biomed. 122 (2021) 104657.

[59] Preuss, M. et al., ASTM Special Technical Publication 1529 STP, pp. 649-681.

[60] Grovenor CRM, Ni N, Hudson D, Yardley SS, Moore KL, Smith GDW, Lozano-Perez S, Sykes JM, Mechanisms of Oxidation of Fuel Cladding Alloys Revealed by High Resolution APT, TEM and SIMS Analysis, MRS Proc. 1383 (2012) 101-112.

[61] Gong W, Zhang H, Wu C, Tian H, Wang X, The role of alloying elements in the initiation of nanoscale porosity in oxide films formed on zirconium alloys, Corros. Sci. 77 (2013) 391-396.

[62] Fa N HJ, Knez M, Scholz R, Hesse D, Nielsch K, Zacharias M, G Sele U, Influence of surface diffusion on the formation of hollow nanostructures induced by the Kirkendall effect: the basic concept., Nano Lett. 7 (2007) 993-997.

[63] Garner A, Hu J, Harte A, Frankel P, Grovenor C, Lozano-Perez S, Preuss M, The effect of Sn concentration on oxide texture and microstructure formation in zirconium alloys, Acta Mater. 99 (2015) 259-272.

[64] Godlewski J, Bouvier P, Lucazeau G, Fayette L, Stress Distribution Measured by Raman Spectroscopy in Zirconia Films Formed by Oxidation of Zr-Based Alloys, In: Moan GD, ed. West Conshohocken, PA: ASTM International, 2000, pp. 877-900.

[65] G. P. Sabol, G. D. Moan, Eds., American Society for Testing and Materials, West Conshohocken, PA, 2000, pp. 877-900

[66] Qin W, Nam C, Li HL, Szpunar JA, Tetragonal phase stability in ZrO2 film formed on zirconium alloys and its effects on corrosion resistance, Acta Mater. 55 (2007) 1695-1701.

[67] Garner A, Gholinia A, Frankel P, Gass M, MacLaren I, Preuss M, The microstructure and microtexture of zirconium oxide films studied by transmission electron backscatter diffraction and automated crystal orientation mapping with transmission electron microscopy, Acta Mater. 80 (2014) 159-171.

[68] Won C, Park J, Ahn K, Yoon J, Effects of abrasive wear and chipping-type abrasive wear on degradation of edge stretchability with advanced high-strength steels, Wear 484-485 (2021) 204031.

[69] Greenwood JA, Williamson JBP, Contact of nominally flat surfaces, Proc. R. Lon., Ser. A 295 (1966) 300-319.

[70] Nikulin SA, Markelov VA, Gusev AY, Nechaykina TA, Rozhnov AB, Rogachev SO, Zadorozhnyy MY, Low-cycle fatigue tests of zirconium alloys using a dynamic mechanical analyzer, Int. J. Fatigue. 48 (2013) 187-191.

[71] Zhang C, Zeng X, Cheng J, Wang Y, Fatigue life improvement and grain growth of gradient nanostructured industrial zirconium during high cycle fatigue, J. Mater. Sci. Technol. 87 (2021) 101-107.

[72] J. Godlewski, P. Bouvier, G. Lucazeau, L. Fayette, Stress distribution measured by raman spectroscopy in zirconia films formed by oxidation of Zr-based alloys. Zirconium in the Nuclear Industry: Twelfth International Symposium, ASTM STP 1354, G. P. Sabol and G. D. Moan (West Conshohocken, PA: ASTM International, 2000), 877-900.